Full Text View

Volume 28, Issue 3 (March 1998)

**Journal of Physical Oceanography**
Article: pp. 433–460 | Abstract | PDF (1.11M)

# Geographical Variability of the First Baroclinic Rossby Radius of Deformation

**Dudley B. Chelton, Roland A. deSzoeke, and Michael G. Schlax**

*College of Oceanic and Atmospheric Sciences, Oregon State University, Corvallis, Oregon*

**Karim El Naggar and Nicolas Siwertz**

*École Polytechnique, Paris, France*

(Manuscript received November 12, 1996, in final form June 23, 1997)

DOI: 10.1175/1520-0485(1998)028<0433:GVOTFB>2.0.CO;2

ABSTRACT

Global 1° × 1° climatologies of the first baroclinic gravity-wave phase speed $c_1$ and the Rossby radius of deformation $\lambda_1$ are computed from climatological average temperature and salinity profiles. These new atlases are compared with previously published 5° × 5° coarse resolution maps of $\lambda_1$ for the Northern Hemisphere and the South Atlantic and with a 1° × 1° fine-resolution map of $c_1$ for the tropical Pacific. It is concluded that the methods used in these earlier estimates yield values that are biased systematically low by 5%–15% owing to seemingly minor computational errors. Geographical variations in the new high-resolution maps of $c_1$ and $\lambda_1$ are discussed in terms of a WKB approximation that elucidates the effects of earth rotation, stratification, and water depth on these quantities. It is shown that the effects of temporal variations of the stratification can be neglected in the estimation of $c_1$ and $\lambda_1$ at any particular location in the World Ocean. This is rationalized from consideration of the WKB approximation.





## 1. Introduction

The first baroclinic Rossby radius of deformation plays a fundamentally important role in extratropical large-scale ocean circulation theory. It defines the length scale of baroclinic variability longer than which internal vortex stretching is more important than relative vorticity. It also figures in the phase and group velocities of baroclinic Rossby-wave solutions to the linear, unforced potential vorticity equation for zero background mean flow. It is intimately related to the dominant length scale of unstable waves in a stratified shear flow.

In consideration of its significance to ocean circulation theory, a reliable, finely resolved, global climatology of the first baroclinic Rossby radius is clearly of great value. Emery et al. (1984) and Houry et al. (1987) published 5° × 5° coarse resolution climatological average maps of the first baroclinic Rossby radius for the Northern Hemisphere and the South Atlantic, respectively. Picaut and Sombardier (1993) published a 1° × 1° fine-resolution map of the first baroclinic gravity-wave phase speed (which is directly proportional to the first baroclinic Rossby radius outside of the equatorial band) for the region 30°N to 30°S in the tropical Pacific. One of the objectives of this study is to extend the results of these three previous studies to the global ocean with a spatial resolution of 1° × 1°.

A fundamental assumption of the linear theory from which the baroclinic Rossby radius of deformation is derived is that effects of temporal variability of the stratification can be neglected. A second objective of this study is to investigate the justification for this assumption by determining the range of first baroclinic Rossby radius values derived from the seasonal cycles of temperature and salinity profiles on the 1° × 1° grid. A large seasonal variation of Rossby radius values at any given location would imply that this aspect of the linearization is invalid.

This study was also motivated by a recent analysis of altimeter data (Chelton and Schlax 1996), which showed large-scale, low-frequency sea level signals propagating westward throughout much of the World Ocean. The space–time character of these features is very similar to that expected for freely propagating, linear, first baroclinic Rossby waves. The phase speeds of long baroclinic Rossby waves are proportional to the square of the baroclinic Rossby radius of deformation. Outside of the Tropics, the observed propagation speeds are systematically higher than the nondispersive Rossby-wave phase speeds predicted on the basis of the Emery et al. (1984) and Houry et al. (1987) estimates of the first baroclinic Rossby radius. The discrepancy is about a factor of 2 at 35° latitude and larger at higher latitudes. A similar discrepancy between observed and predicted propagation speeds has been deduced from upper-ocean thermal data by Kessler (1990). Among several candidate explanations, these results suggest the need for a critical assessment of the accuracy of the previously published estimates of the baroclinic Rossby radius to determine whether the discrepancies are due simply to errors in the estimated Rossby radius.

The formalism for determining the Rossby radii of deformation and an approximate analytical solution for the baroclinic Rossby radii are briefly summarized in section 2; complete derivations are given in appendix A, and the numerical method used to compute the Rossby radii is described in appendixes B and C. Geographical variability in a 1° × 1° global climatology of the first baroclinic Rossby radius is described in section 3. The importance of temporal variability of the stratification in the estimation of the Rossby radius is assessed in section 4. The implications of the results are discussed in section 5.

## 2. The Rossby radii of deformation

It is shown in section a of appendix A that the baroclinic Rossby radii of deformation can be obtained by solving a Sturm–Liouville eigenvalue problem for the vertical structure $\Phi(z)$ of the vertical velocity, which can be written in the form

$$\frac{d^2\phi}{dz^2} + \frac{N^2(z)}{c^2}\phi = 0, \qquad (2.1a)$$

$$\phi = 0 \quad \text{at } z = 0 \qquad (2.1b)$$

$$\phi = 0 \quad \text{at } z = -H, \qquad (2.1c)$$

where $f = 2\Omega \sin\vartheta$ is the Coriolis parameter for earth rotation rate $\Omega$ and latitude $\vartheta$, $H$ is the local mean water depth, and $N^2(z)$ is the squared buoyancy frequency. The surface boundary condition (2.1b) is the rigid-lid approximation, which is valid for the baroclinic solutions of interest here. The bottom boundary condition (2.1c) is for a flat-bottom ocean. Horizontal variations of $f$, $H$, and $N(z)$ are neglected in the formulation of (2.1). However, if these variations are small over a Rossby radius of deformation (see below), then a WKB development in the horizontal shows that (2.1) represents a reasonable local theory.

The eigenvalue problem (2.1) permits an infinite number of ordered, nonnegative eigenvalues $c^{-2}_1 < c^{-2}_2 < c^{-2}_3 < \cdots$ and corresponding eigenfunctions $\Phi_1(z)$, $\Phi_2(z)$, $\Phi_3(z)$, . . . . The subscript $m$ denotes the baroclinic mode number. The eigenvalues and eigenfunctions are estimated by discretizing the continuously stratified eigenvalue equation (2.1) as described in appendix C and solving the resulting system of equations numerically.

It is shown in section b of appendix A that an approximate solution for $c_m$ can be obtained by the WKB method, which gives

$$c_m \approx c_m^{\mathrm{WKB}} = \frac{1}{m\pi}\int_{-H}^{0} N(z)\,dz, \qquad m \geq 1. \qquad (2.2)$$

Physically, the parameter $c_m$ is the phase speed of long, mode-$m$ gravity waves in a nonrotating, continuously stratified fluid (Gill 1982; LeBlond and Mysak 1978). Outside of the Tropics, the Rossby radius of deformation for mode $m$ at latitude $\vartheta$ is determined from $c_m$ by

$$\lambda_m = \frac{c_m}{|f(\vartheta)|} \qquad \text{if } |\vartheta| \gtrsim 5°. \qquad (2.3a)$$

Within the equatorial band, the Rossby radius of deformation can be defined (see Gill 1982) as

$$\lambda_m = \left(\frac{c_m}{2\beta(\vartheta)}\right)^{1/2} \qquad \text{if } |\vartheta| \lesssim 5°, \qquad (2.3b)$$

where $\beta(\vartheta) = df/dy = 2\Omega R_e^{-1} \cos\vartheta$ is the latitudinal variation of the Coriolis parameter for earth radius $R_e$. The WKB approximation for $\lambda_m$ obtained from (2.2) for the region of primary interest here (i.e., outside of the equatorial band) is

$$\lambda_m \approx \lambda_m^{\mathrm{WKB}} = \frac{1}{|f|m\pi} \int_{-H}^{0} N(z)\, dz, \qquad m \geq 1. \qquad (2.4)$$

Several features of the Rossby radii can be inferred from (2.4).

1. The geographical variability of $\lambda_m$ is dominated by an inverse dependence on $|f|$. Thus, $\lambda_m$ decreases with increasing latitude owing to the $\beta$ effect.

2. At a given latitude, $\lambda_m$ is proportional to the vertical integral of $N(z)$ and inversely proportional to the baroclinic mode number $m$. Since the stratification is weak at high latitudes, the dependence on $N(z)$ also results in a decrease of $\lambda_m$ with increasing latitudes poleward of the subtropical gyres in both hemispheres.

3. Because most of the large-scale topographic variations in the open ocean are restricted to the lower half of the water column in which $N(z)$ is small and approximately constant, there is an approximately linear dependence of $\lambda_m$ on water depth $H$.

It can be noted from (2.2) that, unlike the Rossby radii $\lambda_m$, the gravity-wave phase speeds $c_m$ do not depend on $f$. The effects of stratification and water depth on the mode-$m$ eigensolution of (2.1) are thus wholly embodied in the parameter $c_m$.

The WKB solutions $\lambda^{\mathrm{WKB}}_1$ and numerical estimates $\lambda_1$ on a 1° × 1° global grid (see section 3) are compared in Fig. 1. The WKB approximations are, on average, systematically high by about 6.5%. This bias is probably associated with the spike in $N(z)$ profiles often found at the base of the mixed layer (see examples in section b of appendix A). Although this spike violates the conditions for the strict validity of the WKB approximation, (2.4) is nonetheless surprisingly accurate; 68% of the WKB approximations of the first baroclinic Rossby radius of deformation fall within ±9% of the numerical estimates and 95% fall within ±24% of the numerical estimates (Fig. 1b).

Although not sufficiently accurate for many applications, the WKB approximations $c^{\mathrm{WKB}}_1$ and $\lambda^{\mathrm{WKB}}_1$ provide a very useful physical interpretation of the geographical variability of the quantitatively accurate numerical estimates of $c_1$ and $\lambda_1$ presented in sections 3 and 4.

## 3. Geographical variability of the first baroclinic Rossby radius

### *a. Annual mean climatology*

The squared buoyancy frequency profile $N^2(z)$ was estimated from centered first differences of the "neutral density gradient" as described in section d of appendix B based on 1° × 1° gridded climatological average temperature and salinity profiles constructed at standard depths (see Table B1 in appendix B) by the National Oceanographic Data Center (NODC). The details of the NODC climatological average hydrographic dataset are described by Boyer and Levitus (1994), Levitus et al. (1994), and Levitus and Boyer (1994).

Because of the approximately linear dependencies of the baroclinic gravity-wave phase speeds and Rossby radii on water depth, it is important that the full water column be represented in the eigenvalue calculation. An additional discrete depth at the ocean bottom was therefore added to the density profile at each specific 1° × 1° location if the water depth was deeper than the deepest NODC standard depth for that location. The bottom density was taken to be the adiabatically adjusted linear extrapolation of the density values at the two deepest NODC standard depths. This yields an extrapolated deepest value of $N^2(z)$ that is equal to the value calculated from the deepest pair of standard depths.

The first baroclinic gravity-wave phase speed $c_1$ was computed from the discretized $N^2(z)$ profile at each 1° × 1° grid location by discretizing the eigenvalue problem (2.1) as described in section a of appendix C and numerically solving the resulting "layer equations" using a matrix eigenvalue routine. The differential equation was also solved numerically at each grid location using the iterative "shooting method" (Pryce 1993; Press et al. 1992). The root-mean-square difference between the two numerical estimates for $c_1$ over the 1° × 1° global grid was 0.018 m $s^{-1}$, which is typically less than a 1% difference. The close agreement between these two estimates alleviates any concerns about possible inaccuracies resulting from the matrix approach summarized in section a of appendix C, specifically with regard to the discretization interval imposed by the NODC standard depths (Pryce 1993; see also section b of appendix C).

The effects of stratification and water depth inferred from the WKB approximation (2.2) are very evident in the numerical estimates contoured in the map of the annual mean 1° × 1° gridded first baroclinic gravity-wave phase speed $c_1$ shown in Fig. 2.[1] Comparison with the bathymetric shading in the figure reveals that contours of $c_1$ tend to parallel bathymetric contours. Major topographic features such as the Mid-Atlantic Ridge, the East Pacific Rise, the Hawaiian Ridge, the complex of ridges in the Indian Ocean, and numerous smaller ridges and seamount chains throughout the World Ocean are clearly delineated by the locally reduced values of $c_1$ in shallower water.

At subtropical latitudes, the effects of longitudinal variations of the stratification are manifest as the increase of $c_1$ from about 2.4 m $s^{-1}$ near the eastern boundaries to more than 3 m $s^{-1}$ near the western boundary currents. This east–west asymmetry is an indication of stronger stratification in the western basins suggested by the WKB approximation (2.2). As shown by the example in Fig. 3, the basin-scale longitudinal variation of $c_1$ along 24°N across the North Pacific arises because of the deeper permanent pycnocline and corresponding larger vertically integrated $N(z)$, and hence $c^{\mathrm{WKB}}{}_1$, in the western basin in association with the westward intensification of the subtropical gyre. The shorter-scale variations of $c_1$ in Fig. 3 represent the topographic effects noted from the WKB approximation (2.2); the gravity-wave phase speed decreases over shallow water.

In the equatorial Pacific, $c_1$ increases from about 2.2 m $s^{-1}$ off the coast of Ecuador to about 3 m $s^{-1}$ near the date line. As shown in Fig. 4, this zonal variation of $c_1$ reflects the deepening of the pycnocline and an associated larger vertically integrated $N(z)$ and $c^{\mathrm{WKB}}{}_1$ toward the west. The effects of stratification are somewhat masked by topographic effects on $c_1$ west of about 165°E in the Pacific (Fig. 4) and throughout the tropical Atlantic and Indian Oceans (Fig. 2).

At Northern Hemisphere subpolar latitudes, the effects of latitudinal variations of stratification are apparent from the approximate linear decrease of $c_1$ northward across the subpolar gyres to values as low as about 2 m $s^{-1}$ near the Aleutian Islands in the North Pacific and to less than 1 m $s^{-1}$ in the weakly stratified water near Greenland and Iceland in the North Atlantic. In the Southern Hemisphere, $c_1$ decreases linearly southward across the Antarctic Circumpolar Current to values of about 1 m $s^{-1}$ in the weakly stratified water near Antarctica. These effects of latitudinal variations of stratification are also evident in the global zonally averaged values of $c_1$ shown in Fig. 5.

A map of the first baroclinic Rossby radius of deformation $\lambda_1$ computed from the gravity-wave phase speed $c_1$ by (2.3) is shown in Fig. 6. The dominant $|f|^{-1}$ dependence noted from the extratropical WKB solution (2.4) is clearly evident from the predominantly zonal orientations of the contours. The first baroclinic Rossby radius decreases from about 240 km in the near-equatorial band to less than 10 km at latitudes higher than about 60°. The basin-scale longitudinal deviation in Fig. 6 from the strictly zonal contours that a simple $|f|^{-1}$ dependence would imply arises because of the effects of the deeper permanent pycnocline and corresponding larger vertically integrated $N(z)$ in the western basins noted previously from the map in Fig. 2 and the zonal sections in Figs. 3 and 4. The shorter-scale perturbations from strictly zonal contours of $\lambda_1$ near major topographic features are manifestations of the dependence of $\lambda_1$ on water depth also noted previously.

The strong latitudinal dependence of the first baroclinic Rossby radius is also illustrated by the global zonally averaged values of $\lambda_1$ shown in Fig. 7. The equatorial solution (2.3b) is shown between 5°N and 5°S. For practical use in

applications for which a characteristic latitudinal variation of $\lambda_1$ is desired, an analytical expression for the latitudinal variation of the global zonally averaged extratropical baroclinic Rossby radii in Fig. 7 was derived by regression onto a quadratic function of inverse latitude. The resulting global regression fits for each hemisphere separately are shown by the dashed lines in Fig. 7, and the corresponding regression parameters are listed in Table 1. The regression parameters for each individual ocean basin are also listed in Table 1. In the extratropical latitudes where the quasigeostrophic formalism (appendix A) is valid, the root-mean-square errors of the regression fits are less than 2.6 km in all ocean basins except the South Indian where the root-mean-square error is 3.6 km (see Table 1).

The 1° × 1° gridded fields of $c_1$ and $\lambda_1$ presented here are compared with previously published values in section e of appendix B. It is shown that subtle and seemingly minor errors in previous methods result in 5%–15% underestimates of $c_1$ and $\lambda_1$.

### *b. Sensitivity to the density climatology*

The NODC climatological average temperature and salinity profiles from which $N^2(z)$ was estimated for the Rossby radius calculations in this global analysis were constructed by NODC from historical temperature and salinity profiles by isobaric averaging on constant standard-depth pressure surfaces. In addition, the NODC processing included spatial smoothing of the temperature and salinity profiles over horizontal scales of order 1000 km (see, e.g., Table 3 of Levitus and Boyer 1994). (The precise filtering properties of the NODC objective analysis procedure depend on the data distribution near the estimation location.) The resulting climatological description of the hydrography of the World Ocean has become an invaluable resource to ocean modelers and observationalists alike. Indeed, this is the only global hydrographic climatology presently available for analyses such as the global Rossby radius calculation presented here.

While the virtues and utility of the NODC hydrographic dataset are undisputed, an important limitation of the dataset is also widely recognized. The large NODC spatial smoothing, which is essential in data-sparse regions of the ocean (e.g., most of the Southern Hemisphere), broadens the spatial scales of water property distributions in regions of sloping isopycnals. Lozier et al. (1994, 1995) have shown that this problem is further exacerbated by the use of isobaric averaging. Because mixing in the ocean occurs primarily along isopycnal surfaces, spatial gradients of water properties are smaller on isopycnal surfaces than on isobaric surfaces. For a given choice of spatial smoothing, spatial gradients of water properties are thus better retained by averaging and smoothing historical hydrographic data along isopycnal surfaces than by isobaric averaging and smoothing. Lozier et al. (1994) showed that isobaric averaging can actually yield spurious water mass anomalies that are purely artifacts of the isobaric averaging process.

A new 1° × 1° climatological-average North Atlantic hydrographic dataset has recently been constructed by Lozier et al. (1995, referred to hereafter as LOC) based on isopycnal averaging and minimal spatial smoothing over scales on the order of 200 km. Expansions of this dataset to include the South Atlantic and North Pacific are under way. The sensitivity of the Rossby radius calculation presented in section 3a to the density climatology from which $N^2(z)$ is estimated is investigated here by comparison with 1° × 1° Rossby radius estimates computed from the LOC climatological average hydrographic profiles.

North Atlantic maps of the first baroclinic gravity-wave phase speed $c_1$ and Rossby radius $\lambda_1$ computed from the LOC data are shown in Fig. 8. The contours are generally very similar to the North Atlantic contours in Figs. 2 and 6. A scatterplot comparison of $\lambda_1$ computed from the two datasets is shown in Fig. 9a. Over most of the North Atlantic, the two estimates are in very close agreement; 68% of the NODC solutions fall within ±5% of the LOC solutions and 95% fall within ±20% of the LOC solutions (Fig. 9b).

A map of the locations where the NODC and LOC solutions for $\lambda_1$ differ by more than ±10% is shown in Fig. 10. The influences of the effects of isobaric averaging and large horizontal smoothing are readily apparent. By comparison with the dynamic height field superimposed on Fig. 10, it can be seen that most of the large discrepancies are associated with regions of steeply sloping isopycnal surfaces, for example, the Gulf Stream and its northward extension around Grand Banks and Flemish Cap. The LOC values of the Rossby radius are more than 10% larger than the NODC values on the right side (when facing downstream) of this current system. Likewise, the LOC values are 10% smaller than the NODC values on the left side. Locations of more than ±10% differences are also found along the eastern continental margin and more or less randomly distributed over the open ocean poleward of 40°N where $\lambda_1$ becomes very small (less than 20 km) and small differences are therefore a large fraction of the NODC value. Some of these differences are likely attributable to the different quality control procedures applied to the historical hydrographic data.

The differences between estimates of $\lambda_1$ from the LOC and NODC datasets can be understood by consideration of the WKB approximation (2.4). As shown by the example vertical sections of density in Figs. 11a and 11b, the mean Gulf Stream is much broader and less well defined in the NODC data than in the LOC data. As a result, the vertically integrated $N(z)$ and hence, from (2.2), the WKB approximation $c^{\mathrm{WKB}}{}_1$ of the gravity-wave phase speed, are weaker on the equatorward

side of the Gulf Stream in the isobaric averaged and heavily smoothed NODC data (Fig. 11d). As expected from the WKB approximations, the baroclinic gravity-wave phase speed $c_1$ and the Rossby radius $\lambda_1$ are correspondingly higher in the LOC data (Fig. 11e). On the poleward side of the Gulf Stream, isopycnals are all much shallower and the vertically integrated $N(z)$ and $c^{\mathrm{WKB}}{}_1$ are smaller in the LOC data, resulting in smaller values of $c_1$ and $\lambda_1$.

## 4. Effects of temporal variability of the stratification

### *a. Annual variability*

The linearization leading to the eigenvalue problem (2.1) assumes that the effects of temporal variability of the stratification are small. This can be investigated by naively computing the baroclinic gravity-wave phase speed $c_1$ or Rossby radius $\lambda_1$ for each month of a 12-month climatological average seasonal cycle of density profiles and examining the magnitude of the seasonal variations in computed values. The seasonal cycle of $\lambda_1$ has previously been computed in this manner for the North Pacific and North Atlantic by Emery et al. (1984), who concluded that seasonal variability was surprisingly small. The seasonal cycle is investigated here over a larger geographical domain and the small seasonal variability is interpreted in light of the WKB approximation (2.4).

The first baroclinic Rossby radius of deformation was computed from the hydrographic profiles at each of the 1° × 1° grid locations for which the 12-month climatological average seasonal cycle was available in the NODC dataset. Each time series of $\lambda_1$ was then regressed onto an annual cycle with frequency $f_1$ = 1 cycle per year,

$$\hat{\lambda}_1 = A_0 + A_c \cos 2\pi f_1 t + A_s \sin 2\pi f_1 t. \quad (4.1)$$

The amplitude of annual variability is obtained from the regression coefficients $A_c$ and $A_s$ by

$$A_1 = [A^2_c + A^2_s]^{1/2}. \quad (4.2)$$

The residuals from the annual regression fit were very small; 68% of the regression residuals were within ±1% of the corresponding mean Rossby radius and 90% of the residuals were within ±2.5% of the mean Rossby radius. The mean and annual cycle (4.1) are thus a highly accurate description of the seasonally varying Rossby radii.

A map of the constant offset regression coefficient $A_0$ (not shown) is virtually indistinguishable from the map of the annual-mean first baroclinic Rossby radius shown in Fig. 6. The amplitude $A_1$ of annual variability is shown in Fig. 12. These seasonal variations expressed as a percentage of the annual mean $\lambda_1$ in Fig. 6 are exactly equivalent to the amplitudes of seasonal variations of the baroclinic gravity-wave phase speeds $c_1$ expressed as a percentage of the annual mean $c_1$ shown in Fig. 2. Typical values are only 1%–2%. Except for a few bull's eyes of locally large values of $A_1$, a maximum annual variability of about 4% occurs in the eastern tropical Pacific. An inspection of the density profiles in the bull's eyes near 22°S, 75°E in the South Indian Ocean and near 10°N, 125°W in the eastern tropical Pacific concluded that one or more of the 12 monthly mean temperature and salinity profiles in the 1994 NODC climatological average dataset are highly suspect at these locations.

The small annual variability of the baroclinic Rossby radius is easily understood by consideration of the WKB approximations (2.2) and (2.4). Substantial changes of $c_1$ and $\lambda_1$ require large changes of the vertical integral of $N(z)$. Seasonal variations of the density structure are mostly restricted to the upper few hundred meters, which is only a small fraction of the total water column. Although annual variations of $N(z)$ are often very large within the seasonal pycnocline, the effect on the vertical integral of $N(z)$ over the entire water column is small. The net effect on the baroclinic Rossby radii is therefore only a few percent at most.

### *b. Intraseasonal and interannual variability*

The effects of temporal variability of the stratification on the Rossby radius on timescales other than the annual cycle considered in section 4a are of interest. Unfortunately, there are few locations in the World Ocean where a long-term program of repeated hydrographic measurements has been maintained. An upper bound on the importance of temporal variations in the stratification can be obtained by examining $\lambda_1$ for all individual density profiles within, for example, 1°-square areas of the ocean. This was investigated here by computing numerical solutions of the eigenvalue problem for each density profile in the quality-controlled LOC 86-yr historical hydrographic dataset for the North Atlantic.

In order to isolate the effects of temporal variability of the stratification, it is important to eliminate to the extent possible

any effects of spatial variability within each 1°-square area. The effects of geographical variability of the water depth $H$ can be removed by assuring that all of the estimates of $\lambda_1$ within a given 1° square are calculated from density profiles over exactly the same depth range. To this end, only those profiles that extended to a depth of at least 3500 m were considered (see the bathymetric maps in Fig. 8). Furthermore, the portions of any density profiles deeper than 3500 m were excluded from this analysis for the purposes of this calculation. Individual estimates of $c_1$ within each 1° square were thus calculated from profiles of exactly 3500-m depth. The baroclinic Rossby radius $\lambda_1$ for each profile was then obtained from $c_1$ by (2.3) using the value of $f$ or $\beta$ at the center of the 1° square. The resulting values of $\lambda_1$ are still affected by spatial variations of the mean stratification over the 1° areas. This is a particularly important consideration in the interpretation of these results in regions of strong horizontal shear such as the Gulf Stream.

A scatterplot of the individual values of $\lambda_1$ is shown in Fig. 13a as a function of the long-term average $\lambda_1$ computed from the upper 3500 m of the climatological average density profile at the 1° × 1° grid point nearest the sample location. The preponderance of historical North Atlantic hydrographic measurements have been made in the vicinity of the Gulf Stream (see Fig. 2 of Lozier et al. 1995) where $\lambda_1$ ranges between about 20 and 30 km (see Fig. 8b). Some of the scatter in this portion of Fig. 13a can therefore be attributed to the effects of spatial variability of the mean stratification over the 1° squares. The variability in Fig. 13a can thus be considered an upper bound on intraseasonal and interannual variability of the first baroclinic gravity-wave phase speed.

In an attempt to quantify the degree of variability of the Rossby radius, the individual points in Fig. 13a were sorted into 5-km bin sizes according to the climatological average Rossby radius along the abscissa. The root-mean-square differences in kilometers and the root-mean-square percent differences within each 5-km bin are shown in Fig. 13b. As shown in Fig. 13c, the bins with climatological average Rossby radii greater than 40 km are very sparsely sampled compared with bins with average Rossby radii ranging from 10 to 40 km. This again reflects the dense sampling near the Gulf Stream. Although the statistical reliability of the results is highly variable from one bin to another, the results are nonetheless suggestive that the upper bound on the root-mean-square intraseasonal and interannual variability of the first baroclinic Rossby radius is generally less than 10%. At latitudes higher than 40°N, where the climatological average Rossby radius is less than 20 km, the root-mean-square variability is only a few kilometers. The root-mean-square variability increases to about 10 km in the Tropics where the climatological average Rossby radius is more than 100 km.

## 5. Discussion and conclusions

Atlases of the first baroclinic gravity-wave phase speed $c_1$ and Rossby radius of deformation $\lambda_1$ were computed on a global 1° × 1° grid from the NODC climatological average hydrographic dataset produced by Boyer and Levitus (1994). The numerically computed values of $c_1$ and $\lambda_1$ can be obtained via the Internet by contacting the corresponding author by e-mail at chelton@oce.orst.edu. Geographical variations of the climatological averages of $c_1$ and $\lambda_1$ were discussed in the context of a WKB approximation. Although not sufficiently accurate for many applications, the WKB approximation is shown here to be very useful for elucidating the effects of earth rotation, stratification, and water depth on $c_1$ and $\lambda_1$. The geographical variability of $\lambda_1$ is dominated by a latitudinal variation owing to an inverse dependence on the Coriolis parameter $f$. At a given latitude, the baroclinic Rossby radii are approximately proportional to the vertical integral of the buoyancy frequency $N(z)$. The Rossby radii thus increase with increasingly strong stratification and decrease with decreasing water depth. The effects of stratification and water depth are most clearly seen in the geographical distribution of $c_1$, which does not depend on $f$.

The availability of the high-quality LOC climatological average hydrographic dataset produced by Lozier et al. (1995) for the North Atlantic allows an assessment of the sensitivity of the Rossby radius calculation to the particular hydrographic dataset used to estimate $N(z)$ from which the Rossby radius is calculated. The LOC North Atlantic dataset differs significantly from the global NODC dataset used elsewhere in this study. The NODC dataset was constructed by isobaric averaging and large, ~1000 km, spatial smoothing. The LOC dataset was constructed by isopycnal averaging and minimal spatial smoothing of ~200 km on isopycnal surfaces. In regions of sloping isopycnals, the LOC hydrographic fields retain much higher spatial resolution than the NODC fields.

A comparison of $c_1$ and $\lambda_1$ computed from the LOC and NODC climatological average datasets concluded that the calculated values agree to within a few percent over most of the North Atlantic. However, near the Gulf Stream and its northward extension around Grand Banks and Flemish Cap, the LOC and NODC estimates of these parameters differ by more than 10%. It can thus be concluded that the global atlases of $c_1$ and $\lambda_1$ presented in Figs. 2 and 6 are generally accurate to within a few percent, except near intense currents that are overly smoothed in the NODC hydrographic dataset.

The WKB approximation also elucidates the insignificance of temporal variations of stratification on $c_1$ and $\lambda_1$. Seasonal variations of the density profile are mostly restricted to the upper few hundred meters of the water column. While these seasonal variations have a very strong effect on $N(z)$ locally near the depth of the seasonal pycnocline, their effect on the vertical integral of $N(z)$ and hence $c^{\mathrm{WKB}}$ is relatively small. Seasonal variations of $c$ and $\lambda$ are therefore only a few

percent at most.

Quantitative estimates of the importance of temporal variability of the stratification on other timescales (intraseasonal and interannual) in the estimation of $c_1$ and $\lambda_1$ are difficult to obtain because of the lack of hydrographic time series at fixed locations. It was shown from an analysis of the 1°-gridded LOC historical hydrographic data in the North Atlantic that an upper bound on temporal variability is less than 10%. Much of this variability can undoubtedly be attributed to spatial variations of the mean stratification over the 1°-square areas. It is concluded that the effects of temporal variations of the stratification can be neglected for the purposes of estimating $c_1$ and $\lambda_1$.

As noted in the introduction, one of the objectives of this study was to determine whether systematic errors in previously published atlases of the Rossby radius could account for the apparent factor-of-2 discrepancy between the westward propagation speeds of midlatitude sea level signals observed in TOPEX/POSEIDON altimeter data by Chelton and Schlax (1996) and the phase speeds predicted from the standard theory for nondispersive Rossby waves. A quantitative, detailed comparison with previous atlases of the first baroclinic Rossby radius published by Emery et al. (1984), Houry et al. (1987), and Picaut and Sombardier (1993) concluded that the previous estimates are indeed biased systematically low (see section e of appendix B). The errors in the previous published results can be attributed to seemingly minor errors in the details of the methods used to compute the Rossby radius. In particular, the use of the gradient of potential density (rather than the neutral density gradient defined in section d of appendix B) to estimate $N^2(z)$ and/or the use of forward first differences (rather than centered first differences) yields first baroclinic Rossby radii that are biased 5%–15% low. The precise geographical distribution of the bias depends on the water masses sampled by the hydrographic profiles.

The phase speeds $c^p{}_1$ of extratropical long, baroclinic Rossby waves are related to the Rossby radius $\lambda_1$ by $c^p{}_1 = -\beta\,\lambda^2{}_1$. A 10% underestimate of $\lambda_1$ thus corresponds to approximately a 20% underestimate of $c^p{}_1$. Although the 5%–15% biases in previously published atlases of the Rossby radius are significant, they are not of sufficient magnitude to account for the ~ 100% underestimate of midlatitude Rossby wave propagation speeds observed in altimeter data by Chelton and Schlax (1996). The standard theory is evidently deficient in predicting the observed propagation speeds.

Numerous studies are under way to determine the effects on propagation speeds when the linearized potential vorticity equation includes terms omitted from the standard derivation presented in section a of appendix A. White (1977), White et al. (1998), and Qui et al. (1997) have suggested that the apparent speedup is due to a misinterpretation of the propagating signals in altimeter data as freely propagating Rossby waves. With appropriate phasing between narrowband (in frequency) propagating waves and zonally coherent wind forcing, an apparent speedup of a factor of 2 can be obtained. Killworth et al. (1997), deSzoeke and Chelton (1997, manuscript submitted to *J. Phys. Oceanogr.*), and Dewar (1997, manuscript submitted to *J. Phys. Oceanogr.*) have shown that latitudinally varying increases in phase speed very comparable to those observed by Kessler (1990) and Chelton and Schlax (1996) can be obtained for purely free waves when the effects of vertical shear on the potential vorticity field are included in the eigenvalue problem for $\lambda_1$ and $c_1$. Distinguishing between these and other potential mechanisms for the observed increased propagation speeds of long Rossby waves remains a significant challenge.

*Acknowledgments*

We thank Sydney Levitus and Tim Boyer for providing the historical CTD data by Internet ftp to supplement the incomplete vertical profiles contained on the original CD-ROM release of the NODC hydrographic data archive. We also thank Ruth Curry for providing the LOC climatological average and raw density profiles for the North Atlantic used in section 3c. This research was supported by Contract 958127 from the Jet Propulsion Laboratory funded under the TOPEX/POSEIDON Announcement of Opportunity, by Grants NAGW-3510 and NAGW-3051 from the National Aeronautics and Space Administration, and by Grant OCE-9402891 from the National Science Foundation.

---

## REFERENCES

Boyer, T., and S. Levitus, 1994: Quality control and processing of historical oceanographic temperature, salinity and oxygen data. National Oceanic and Atmospheric Administration Tech. Rep. NESDIS 81, U.S. Department of Commerce, 64 pp..

Chelton, D. B., and M. G. Schlax, 1996: Global observations of oceanic Rossby waves. *Science*, **272,** 234–238..

Dewar, W. K., 1998: On “too-fast” baroclinic planetary waves in the general circulation. *J. Phys. Oceanogr.*, in press..

Emery, W. J., and J. S. Dewar, 1982: Mean temperature-salinity, salinity-depth and temperature-depth curves for the North Atlantic and North Pacific. *Progress in Oceanography*, Vol. 11, Pergamon, 219–305..

— , W. G. Lee, and L. Magaard, 1984: Geographic and seasonal distributions of Brunt–Väisälä frequency and Rossby radii in the North Pacific and North Atlantic. *J. Phys. Oceanogr.*, **14,** 294–317..

Gill, A. E., 1982: *Atmosphere–Ocean Dynamics.* Academic Press, 662 pp..

Houry, S., E. Dombrowsky, P. DeMey, and J.-F. Minster, 1987: Brunt–Väisälä and Rossby radii in the South Atlantic. *J. Phys. Oceanogr.*, **17,** 1619–1626..

Kessler, W. S., 1990: Observations of long Rossby waves in the northern tropical Pacific. *J. Geophys. Res.*, **95,** 5183–5217..

Killworth, P. D., D. B. Chelton, and R. A. deSzoeke, 1997: The speed of observed and theoretical long extratropical planetary waves. *J. Phys. Oceanogr.*, **27,** 1946–1966..

LeBlond, P. H., and L. A. Mysak, 1978: *Waves in the Ocean.* Elsevier, 602 pp..

Levitus, S., 1982: *Climatological Atlas of the World Ocean.* National Oceanic and Atmospheric Administration Prof. Paper 13, U.S. Department of Commerce, 173 pp..

— , and T. P. Boyer, 1994: *World Ocean Atlas 1994,* Vol. 4. *Temperature.* National Oceanic and Atmospheric Administration Atlas NESDIS 4, U.S. Department of Commerce, 117 pp..

— , R. Burgett, and T. P. Boyer, 1994: *World Ocean Atlas 1994.* Vol. 3: *Salinity.* National Oceanic and Atmospheric Administration Atlas NESDIS 3, U.S. Department of Commerce, 99 pp..

Lozier, M. S., M. S. McCartney, and W. B. Owens, 1994: Anomalous anomalies in averaged hydrographic data. *J. Phys. Oceanogr.*, **24,** 2624–2638..

— , W. B. Owens, and R. G. Curry, 1995: The climatology of the North Atlantic. *Progress in Oceanography,* Vol. 36, Pergamon, 1–44..

Lynn, R. J., and J. L. Reid, 1968: Characteristics of circulation of deep and abyssal waters. *Deep-Sea Res.*, **15,** 577–598..

Morse, P. M., and H. Feshbach, 1953: *Methods of Theoretical Physics.* McGraw-Hill, 997 pp..

Picaut, J., and L. Sombardier, 1993: Influence of density stratification and bottom depth on vertical mode structure functions in the tropical Pacific. *J. Geophys. Res.*, **98,** 14727–14737..

Press, W. H., S. A. Teukolsky, W. T. Vetterling, and B. P. Flannery, 1992: *Numerical Recipes in Fortran: The Art of Scientific Computing.* Cambridge University Press, 963 pp..

Price, J. F., and M. O'Neil Baringer, 1994: Outflows and deep water production by marginal seas. *Progress in Oceanography,* Vol. 33, Pergamon, 161–200..

Pryce, J. D., 1993: *Numerical Solution of Sturm-Liouville Problems.* Clarendon Press, 322 pp..

Qiu, B., W. Miao, and P. Müller, 1997: Propagation and decay of forced and free baroclinic Rossby waves in off-equatorial oceans. *J. Phys. Oceanogr.*, **27,** 2405–2417..

UNESCO, 1981: Tenth Report of the Joint Panel on Oceanographic Tables and Standards. UNESCO Tech. Pap. Mar. Sci., Vol. 37, 144 pp. [Available from UNESCO Publishing, 1, rue Miollis, 75732, Paris Cedex 15, France.].

White, W., 1977: Annual forcing of baroclinic long waves in the North Pacific Ocean. *J. Phys. Oceanogr.*, **7,** 50–61..

White, W. B., Y. Chao, and C.-K. Tai, 1998: Coupling of biennial oceanic Rossby waves with the overlaying atmosphere in the Pacific basin. *J. Phys. Oceanogr.*, in press..

---

## APPENDIX A

### 6. The Eigenvalue Problem

#### *a. Mathematical formalism*

The standard method for determining the Rossby radii of deformation is to linearize the quasigeostrophic potential vorticity equation about a zero background mean flow. In the absence of buoyancy forcing, wind stress, or frictional forces, the resulting equation (e.g., Gill 1982; LeBlond and Mysak 1978) is a wave equation for freely propagating linear waves. For a flat bottom, the vertical dependence is separable from the horizontal and temporal dependencies. The vertical velocity $w$, for example, can then be expressed as

$$w(x, y, z, t) = \Phi(z)W(x, y, t). \quad \text{(A.1)}$$

Substituting (A.1) into the linearized quasigeostrophic potential vorticity equation and separating the $z$-dependent terms from the $x$-, $y$- and $t$-dependent terms yields the coupled pair of equations

$$\frac{\partial}{\partial t}\left(\nabla_h^2 - \frac{f^2}{c^2}\right)W + \beta\frac{\partial W}{\partial x} = 0 \qquad \text{(A.2)}$$

$$\frac{d^2\phi}{dz^2} + \frac{N^2(z)}{c^2}\phi = 0, \qquad \text{(A.3)}$$

where $c^{-2}$ is the separation constant, $\nabla^2_h = \partial^2/\partial x^2 + \partial^2/\partial y^2$ is the horizontal Laplacian operator, $f = 2\Omega \sin\vartheta$ is the Coriolis parameter at latitude $\vartheta$ for earth rotation rate $\Omega = 7.29 \times 10^{-5}$ s$^{-1}$, $\beta = df/dy = 2\Omega R_e^{-1} \cos\vartheta$ is the latitudinal variation of the Coriolis parameter, $R_e = 6371$ km is the earth's radius, and $N^2$ is the squared buoyancy frequency defined in terms of the water density $\rho$ and sound speed $c_s$ as

$$N^2(z) = -\frac{g}{\rho}\frac{\partial \rho}{\partial z} - \frac{g^2}{c_s^2}. \qquad \text{(A.4)}$$

For present purposes, the second term can be neglected since the sound speed is essentially infinite. The rigid-lid and flat-bottom boundary conditions applicable to the baroclinic solutions of interest here are that the vertical velocity vanish at the sea surface and ocean bottom;that is,

$$\phi = 0 \quad \text{at } z = 0 \qquad \text{(A.5a)}$$

$$\phi = 0 \quad \text{at } z = -H, \qquad \text{(A.5b)}$$

where $H$ is the mean water depth.

The ordinary differential equation (A.3) and boundary conditions (A.5) for the vertical structure of the vertical velocity constitute an eigenvalue problem of Sturm–Liouville form. There is a countable set of increasing nonnegative eigenvalues $c^{-2}_m$ and corresponding eigenfunctions $\Phi_m(z)$. The subscript $m$ labels the different eigensolutions for the normal modes of the coupled equations. The eigenfunction $\Phi_m(z)$ has $m + 1$ intersections with the zero axis, including those at $z = 0$ and $z = -H$. The eigenfunctions satisfy the orthogonality condition

$$\int_{-H}^{0} N^2(z)\phi_k\phi_m \, dz = 0 \quad \text{if } k \neq m. \qquad \text{(A.6)}$$

The eigenvalue problem (A.3) and (A.5) can be recognized as equivalent to the differential equation and boundary conditions for the vertical structure of the vertical velocity for long, baroclinic gravity waves in a nonrotating, continuously stratified fluid. Physically, the parameter $c_m$ is the phase speed of the mode-$m$ gravity wave. At latitudes outside of the Tropics, the Rossby radius of deformation for mode $m$ is obtained from $c_m$ by

$$\lambda_m = \frac{c_m}{|f|} \qquad \text{if } \vartheta \gtrsim 5°. \qquad \text{(A.7a)}$$

Near the equator where $f \longrightarrow 0$, the modified radius of deformation is

$$\lambda_m^{EQ} = \left(\frac{c_m}{2\beta}\right)^{1/2}, \qquad \text{if } \vartheta \lesssim 5° \qquad \text{(A.7b)}$$

(Gill 1982).

The eigenvalue problem (A.3) depends only on $N^2(z)$, which, in turn, requires knowledge of only the local vertical stratification according to (A.4). The method used here to compute $N^2(z)$ from hydrographic data is presented in section d of appendix B. The eigensolutions for a general profile of $N^2(z)$ can be estimated by discretization and numerical solution of (A.3) subject to the boundary conditions (A.5), as summarized in appendix C. Estimates of $c_1$ and $\lambda_1$ are obtained

numerically in section 3a on a 1° × 1° global grid.

*b. WKB approximation*

Although not sufficiently accurate for many applications, insight regarding the nature of the parameters $c_m$ and $\lambda_m$ and the corresponding eigenfunctions $\Phi_m(z)$ can be gained from an analytical approximate solution of the ordinary differential equation (A.3) with boundary conditions (A.5) obtained by the so-called WKB method (Morse and Feshbach 1953). From the form of (A.3), we expect solutions to oscillate with $z$. The WKB method makes the formal substitution

$$\Phi(z) = e^{i\chi(z)}, \tag{A.8}$$

where $\chi(z)$ is the phase of the complex oscillation as a function of $z$. Substituting (A.8) into (A.3) and using primes to denote differentiation with respect to $z$ transforms (A.3) into

$$-\frac{\chi'^2}{\tilde{N}^2} + 1 = -i\frac{\chi''}{\tilde{N}^2}, \tag{A.9}$$

where

$$\tilde{N}^2(z) = \frac{N^2(z)}{c^2}. \tag{A.10}$$

Note that $\Re[\chi'(z)]$ is the (variable) vertical wavenumber of $\Phi$ and $\Re[\chi'/\tilde{N}]$ is this wavenumber scaled by the internal length scale $[\tilde{N}(z)]^{-1}$. In the WKB approximation, the scaled rate of change of vertical wavenumber $\chi''/\tilde{N}^2$ on the right side of (A.9) is assumed to be small compared to the scaled vertical wavenumber, $\chi'/\tilde{N}$, that appears on the left side of the equation.

The WKB approximation considers a series expansion of the form

$$\chi = \chi_0 + \chi_1 + \cdots. \tag{A.11}$$

It is supposed that

$$\frac{\chi_k}{\chi_{k-1}} = O\left(\frac{\chi_0''}{\tilde{N}^2}\right) \lesssim 1, \quad \text{for } k = 1, 2, \cdots \tag{A.12}$$

so that, when (A.11) is substituted into (A.9), an ordered set of equations for the $\chi^k$ is obtained:

$$\frac{\chi_0'^2}{\tilde{N}^2} = 1 \tag{A.13a}$$

$$2\chi_0'\chi_1' = i\chi_0'', \tag{A.13b}$$

$$\cdots.$$

It is evident from (A.13a) that the vertical wavenumber is approximately $\tilde{N}(z)$. The solution for the first term in the expansion (A.11) is easily seen to be

$$\chi_0(z) = \pm \int_{-H}^{z} \tilde{N}(z')\, dz' \tag{A.14}$$

to within an arbitrary additive constant that, from (A.8), corresponds to a multiplicative constant in $\Phi$. The two sign possibilities in (A.4) can be superposed to construct from (A.8) either sine- or cosine-like behavior for the zero-order WKB term of $\Phi$,

where $A = a + b$ and $B = i(a - b)$ are arbitrary constants.

From (A.4), it is seen that $|\chi''_0/\tilde{N}^2| = |\tilde{N}'/\tilde{N}^2|$. The requirement (A.12) that $\chi''_0/\tilde{N}^2$ be small thus also demands that the environment, characterized by the length scale $[\tilde{N}(z)]^{-1}$, change slowly in the vertical.

The next higher-order term in the expansion (A.11) is obtained from (A.13b) using (A.13a):

$$\chi_1' = \frac{i}{2}\frac{\chi_0''}{\chi_0'} = \frac{i}{2}(\ln\chi_0')' = \frac{i}{2}(\ln\tilde{N})'.$$

The integral of this is

$$\chi_1(z) = \frac{i}{2}\ln\tilde{N}(z) \qquad \text{(A.16)}$$

to within another arbitrary additive constant that can be absorbed into $A$ and $B$. Hence,

$$e^{i\chi_1} = [\tilde{N}(z)]^{-1/2}. \qquad \text{(A.17)}$$

Retaining only the first two terms (A.15) and (A.17) in the expansion (A.11), the WKB approximation of (A.8) becomes

$$\phi^{\text{WKB}}(z) = [\tilde{N}(z)]^{-1/2}\left[A\cos\left(\int_{-H}^{z}\tilde{N}\,dz'\right) + B\sin\left(\int_{-H}^{z}\tilde{N}\,dz'\right)\right].$$

The bottom boundary condition (A.5) implies that $A = 0$. Substituting for $\tilde{N}(z)$ from (A.10), the WKB approximation for the mode-$m$ baroclinic vertical velocity eigenfunction is

$$\phi_m \approx \phi_m^{\text{WKB}}(z) = \left[\frac{N(z)}{c_m}\right]^{-1/2} B\sin\left(\frac{1}{c_m}\int_{-H}^{z}N(z')\,dz'\right), \qquad m \geq 1. \qquad \text{(A.18)}$$

The parameter $c^{\text{WKB}}_m$ corresponding to the WKB baroclinic eigenfunction (A.18) is easily determined by applying the rigid-lid boundary condition (A.5) to (A.18). This leads to

$$\sin\left(\frac{1}{c_m}\int_{-H}^{0}N(z')\,dz'\right) = 0,$$

which implies that

$$c_m \approx c_m^{\text{WKB}} = \frac{1}{m\pi}\int_{-H}^{0}N(z')\,dz' \qquad m \geq 1. \qquad \text{(A.19)}$$

From (A.7a), the WKB approximations for the baroclinic Rossby radii of deformation outside of the equatorial band are

$$\lambda_m \approx \lambda_m^{\text{WKB}} = \frac{1}{|f|m\pi}\int_{-H}^{0}N(z')\,dz' \qquad m \geq 1. \qquad \text{(A.20)}$$

The nature of the eigenfunctions can be assessed from the form of (A.18). The amplitude of each baroclinic vertical velocity eigenfunction at depth $z$ is proportional to $[N(z)]^{-1/2}$. The vertical velocity eigenfunctions therefore have smaller amplitude in the upper water column where the stratification is stronger than in the weakly stratified deep water. The eigenfunctions oscillate vertically with a stretched sinusoidal structure that has a local wavelength proportional to $N(z)$. The vertical structure therefore varies more rapidly in the upper water column than in the deep water.

The accuracy of the WKB approximation is illustrated in Fig. A.1 for the first two baroclinic modes from long-term average density profiles at three locations in the middle of the North Atlantic by comparison with solutions of (A.3) and (A.5) computed numerically as described in appendix C. It is apparent that the differences between the WKB and numerical eigenfunctions are largest in the upper water column where the vertical scale of $N(z)$ is short. This is consistent with the WKB assumptions that restrict the validity of the approximation to regions of the water column where the scaled rate of change of the environment [i.e., the vertical derivative of $N(z)$, scaled appropriately as in (A.10)] is small compared with the scaled vertical wavenumber of the eigenfunction. These assumptions are violated in the upper ~ 300 m of the water column where $N(z)$ increases rapidly from a small value near the surface to a maximum at the base of the mixed layer and then decreases rapidly below the mixed layer.

The WKB eigenvalues are less sensitive than the WKB eigenfunctions to the validity of the assumptions of the WKB approximation. For the three locations shown in Fig. A1, the WKB approximations for the first baroclinic Rossby radii all agree with the numerical estimates to within 10%. The relationship between $\lambda_1$ and $\lambda^{\mathrm{WKB}}{}_1$ is examined globally in section 2. The ~ 10% uncertainty of the WKB approximation is too large for many quantitative applications of the baroclinic Rossby radii. However, as shown in sections 3 and 4, the WKB solution provides a very useful interpretation of geographical and temporal variations of the numerical estimates of $\lambda_1$ and $c_1$.

---

## APPENDIX B

### 7. Estimation of the Buoyancy Frequency Profile

It is shown in appendix A that the only information required to compute the first baroclinic gravity-wave phase speed $c_1$ and Rossby radius of deformation $\lambda_1$ is the vertical stratification in order to specify the squared buoyancy frequency profile (A.4) in the differential equation (A.3). We are aware of only three previous studies in which the geographical variability of $c_1$ and $\lambda_1$ over ocean basin scales has been presented. The methods used to estimate $N^2(z)$ in these previous studies are briefly reviewed in sections a, b, and c of this appendix and attention is drawn to inherent weaknesses in all of these methods. An improved method is introduced in section d of this appendix. The sensitivity of $\lambda_1$ to the method used to estimate $N^2(z)$ is illustrated in section e of this appendix and section b of appendix C.

#### *a. The potential density method*

Long-term average potential temperature (denoted as $\theta$) and salinity profiles were compiled by Emery and Dewar (1982) on a 5° × 5° grid of the Northern Hemisphere. These climatological average profiles extended from the surface to a depth of 3000 m at 66 nonuniformly spaced standard depths with higher vertical resolution in the upper water column where temperature and salinity vary most rapidly. For the purposes of estimating $N^2(z)$, Emery et al. (1984) computed an average potential density profile $\rho_\theta(z)$ for each gridded pair of standard-depth, 3000-m potential temperature and salinity profiles. The potential density of a water parcel is defined to be the density that the parcel would have when moved adiabatically from its in situ pressure to atmospheric pressure at the sea surface.

An estimate of the squared buoyancy frequency profile (A.4) was obtained by Emery et al. (1984) by smoothing the potential density profile and then first differencing. Details of the first differencing were not described; as illustrated in section b of appendix C, the first baroclinic Rossby radius calculated from $N^2(z)$ is sensitive to the method used to approximate the density derivative in (A.4). We have assumed that the centered first difference method was used, in which case $N^2(z)$ is estimated from the discrete standard-depth data by

$$N^2(z_{k+1/2}) = -\frac{g}{\rho_0}\left[\frac{\rho_\theta(z_k) - \rho_\theta(z_{k+1})}{z_k - z_{k+1}}\right], \qquad \text{(B.1)}$$

where $z_{k+1/2} \equiv (z_k + z_{k+1})/2$ is the midpoint between standard depths $z_k$ and $z_{k+1}$ (Fig. B.1). The usual positive

upward convention for the $z$ axis has been adopted here so that $z_k > z_{k+1}$. The buoyancy frequency calculated by (B.1) is therefore positive when $\rho_\theta(z_{k+1}) > \rho_\theta(z_k)$. For 5° squares where the 3000-m hydrographic profiles did not extend to the bottom, Emery et al. (1984) linearly extrapolated $N^2(z)$ from 3000 m to a value of $N^2(z) = 0$ at the bottom, $z = -H$.

A weakness of the potential density method is that potential density is not an accurate indicator of $N^2(z)$. Because of the so-called thermobaric effect of the increased compressibility of seawater with decreasing temperature (Lynn and Reid 1968; Price and O'Neil Baringer 1991), $N^2(z)$ computed from $\rho_\theta(z)$ is systematically low. As shown in Fig. B.2, the bias is largest in the deep water column where the water temperatures are coldest. Lynn and Reid (1968) showed that $N^2(z)$ in deep water calculated from potential density can, in fact, be negative, even though the adiabatically adjusted in situ density $\rho(z_{k+1})$ is greater than $\rho(z_k)$.

From the WKB approximations (A.19) and (A.20), the baroclinic Rossby radii are, to a close degree of approximation, proportional to the vertical integral of $N(z)$. The errors from the use of potential density $\rho_\theta$ to estimate $N^2(z)$ are small at any particular depth. However, these errors are systematic and integrate to values of $c_1$ and $\lambda_1$ that are typically biased low by 4%–12%. The geographical variability of this bias is discussed in section e of this appendix.

### *b. The forward first difference method*

Spatially smoothed long-term average temperature and salinity profiles were compiled by Levitus (1982) on a 1° × 1° global grid. These climatological average profiles extended to the bottom at 33 nonuniformly spaced standard depths between the surface and 5500 m (see Table B1) with additional standard depths below 5500 m for the deeper profiles. Houry et al. (1987) averaged the Levitus (1982) 1°-gridded profiles onto a 5° × 5° grid for the South Atlantic and portions of the North Atlantic and Indian Oceans.

In a significant improvement over the potential density method (B.1), Houry et al. (1987) estimated the vertical density gradient in (A.4) in situ with an adiabatic correction, rather than at atmospheric pressure at the sea surface from the vertical gradient of potential density. This avoids the problem of the thermobaric effect discussed in section a of this appendix. Profiles of in situ density $\rho(z)$ were computed from the 5°-gridded in situ temperature and salinity profiles. Houry et al. (1987) then obtained an estimate of the squared buoyancy frequency profile (A.4) by adiabatically adjusting the densities at neighboring standard depths to a common local reference depth, rather than to the sea surface as in the potential density method. For standard depths $z_k$ and $z_{k+1}$, Houry et al. (1987) estimated the buoyancy frequency as forward first differences,

$$N^2(z_k) = -\frac{g}{\rho_0}\left[\frac{\rho(z_k) - \rho(z_{k+1} \rightarrow z_k)}{z_k - z_{k+1}}\right], \qquad \text{(B.2)}$$

where $\rho(z_{k+1} \rightarrow z_k)$ is shorthand notation for the density that a water parcel at $z_{k+1}$ has when moved adiabatically to the next shallower standard depth $z_k$.

Although (B.2) eliminates errors of $N^2(z)$ owing to the thermobaric effect, there are two correctable weaknesses in the forward first difference method. The first is that the water parcel at depth $z_{k+1}$ was raised adiabatically to $z_k$, rather than moving both parcels adiabatically to the midpoint $z_{k+1/2}$. This is a relatively minor point that does not significantly affect the estimate of $N^2(z)$ since the standard depths in the Levitus (1982) climatological-average dataset are closely spaced in the upper water column where $\rho(z)$ varies most rapidly.

The other weakness in the forward first difference method is much more serious. By assigning the first difference on the right side of (B.2) to $N^2$ at depth $z_k$ by forward first differencing, rather than to the correct midpoint depth $z_{k+1/2}$ as in centered first differencing, the $N^2(z)$ profile is effectively shifted upward in the water column (see Fig. B.2). Since $N^2(z)$ decreases monotonically with increasing depth over most of the water column, this estimate of $N^2(z_k)$ is generally biased low. The bias is small if the discrete samples $\rho(z_k)$ are closely spaced, as they are in the upper water column. However, in the lower permanent pycnocline (depths from about 700 m to about 1500 m), where the standard depth spacing in the Levitus (1982) and 1994 NODC climatological-average datasets is 100 m (Table B1) and the vertical variation of $N^2(z)$ is large, the bias introduced by vertically shifting the $N^2(z)$ profile is substantial (see Fig. B2). Accordingly, as predicted from the WKB solutions (A.19) and (A.20), this results in values of $c_1$ and $\lambda_1$ that are biased low. As shown in section b of

appendix C, the bias depends on the vertical spacing of the density samples and the structure of the stratification and is typically 4%–9% for the Levitus (1982) and 1994 NODC standard depth spacing. The geographical variability of this bias is discussed in section e of this appendix.

### *c. The hybrid method*

Picaut and Sombardier (1993) computed the internal gravity-wave phase speed $c_1$ from the eigenvalue equation (2.1) for the latitude range 30°N to 30°S in the Pacific. Numerical estimates for $c_1$ were obtained from $N^2(z)$ profiles derived from the Levitus (1982) 1° × 1° climatological average standard-depth temperature and salinity profiles.

The details of the method used by Picaut and Sombardier to estimate $N^2(z)$ combines to estimate the negative attributes of both the potential density method and the forward first difference method: the $N^2(z)$ profile was estimated by forward first differencing standard-depth profiles of potential density,

$$N^2(z_k) = -\frac{g}{\rho_0}\left[\frac{\rho_\theta(z_k) - \rho_\theta(z_{k+1} \rightarrow z_k)}{z_k - z_{k+1}}\right] = -\frac{g}{\rho_0}\left[\frac{\rho_\theta(z_k) - \rho_\theta(z_{k+1})}{z_k - z_{k+1}}\right]. \quad \text{(B.3)}$$

It can be noted that the right sides of (B.1) and (B.3) are identical. The hybrid method is therefore equivalent to computing the same potential density gradients as the potential density method, except that the resulting first differences in (B.3) are assigned to the upper depths $z_k$ rather than the midpoint depths $z_{k+1/2}$ as in (B.1). From the discussion in sections a and b of this appendix, the resulting estimates of $N^2(z)$ are biased even lower than the estimates obtained by either the potential density method or the forward first difference method. It can therefore be anticipated that the hybrid estimates of $c_1$ are biased low. This is confirmed in section e of this appendix.

### *d. The neutral density gradient method*

For the purposes of this study, the systematic errors of the potential density method, forward first difference method, and hybrid method were ameliorated by modifying (B.2) to estimate $N^2(z)$ by centered first differences of the in situ density, adiabatically adjusted to the midpoint between standard depths,

$$N^2(z_{k+1/2}) = -\frac{g}{\rho_0}\left[\frac{\rho(z_k \rightarrow z_{k+1/2}) - \rho(z_{k+1} \rightarrow z_{k+1/2})}{z_k - z_{k+1}}\right], \quad \text{(B.4)}$$

where, using the notation introduced in section b of this appendix, the terms in the numerator on the right side of (B.4) represent the densities that water parcels at standard depths $z_k$ and $z_{k+1}$ have when moved adiabatically to the midpoint $z_{k+1/2}$. The quantity in square brackets in (B.4) is referred to here as the "neutral density gradient." Adiabatically adjusted densities were computed using the UNESCO (1981) equation of state.

The density profiles used to estimate $N^2(z)$ by (B.4) were computed from the 1° × 1° average temperature and salinity profiles recently produced by NODC, which are described in detail by Boyer and Levitus (1994), Levitus et al. (1994), and Levitus and Boyer (1994). The historical dataset used to construct this new 1° × 1° climatological average hydrographic dataset is significantly expanded from that used to construct the earlier Levitus (1982) climatology.

As shown by the example in Fig. B2, the $N(z)$ profile estimated by (B.4) is higher throughout the water column than the estimate obtained by the potential density method (B.1). It is also higher throughout most of the water column than the estimate obtained by the forward first difference method (B.2).

### *e. Comparison of the four methods*

Contour maps of $c_1$ and $\lambda_1$ computed numerically as described in appendix C based on $N^2(z)$ estimated from the neutral

density gradient by (B.4) are shown in Figs. 2 and 6, respectively, and are discussed in detail in section 3a. These results are compared with previously published results in this section.

The geographical variability of differences between the Rossby radii shown in Fig. 6 and Rossby radii computed by the potential density method (B.1) applied to the 1994 NODC hydrographic data is shown in Fig. B3a, and a histogram of these differences is shown in Fig. B4a. From (A.7), these differences expressed as a percentage of the values of $\lambda_1$ shown in Fig. 6 are exactly equivalent to the differences between the two estimates of the baroclinic gravity-wave phase speed expressed as a percentage of the values of $c_1$ shown in Fig. 2. Because of the thermobaric effect of the temperature dependence of the compressibility of seawater (see section a of this appendix), the biases of $\lambda_1$ and $c_1$ computed by the potential density method are greater than 10% throughout most of the North Atlantic. This is because of the influences of North Atlantic Deep Water and Mediterranean Water. The biases also exceed 10% at high southern latitudes where Antarctic Bottom Water is formed and advected around the Antarctic continent. Elsewhere, the biases generally range between 4% and 8%.

Although the potential density method is clearly flawed, it is important to point out that the errors in the actual maps of $\lambda_1$ published by Emery et al. (1984) differ from those shown in Fig. B3a. In particular, the errors in the North Atlantic are generally somewhat smaller than indicated by Fig. B3a. The actual errors are shown in Fig. B3b. The differences between Figs. B3a and B3b are most likely attributable to the different climatological average hydrographic datasets used in the two calculations.

A quantitative comparison of the 1994 NODC dataset used here and the Emery and Dewar (1982) dataset used by Emery et al. (1984) is beyond the scope of this study. However, it can be noted that, in addition to the much larger number of historical hydrographic profiles in the 1994 NODC dataset, a major difference between the two climatological average hydrographic datasets is that the Emery and Dewar (1982) temperature and salinity profiles extended only to a depth of 3000 m. In order to compute $\lambda_1$, Emery et al. (1984) extrapolated their $N^2(z)$ profiles from 3000 m to a value of zero at the ocean bottom. These extrapolations tend to offset the errors in the use of potential density since the thermobaric effect is generally most pronounced in water deeper than 3000 m. The physical basis for the errors in Fig. B3a is therefore less pronounced in the actual Emery et al. (1984) estimates of the Rossby radii than in the Rossby radii computed here by the potential density method.

The geographical variability of the differences between the Rossby radii shown in Fig. 6 and Rossby radii estimated by the forward first difference method (B.2) applied to the 1994 NODC hydrographic data is shown in Fig. B5, and a histogram of these differences is shown in Fig. B4b. The systematic low bias of $\lambda_1$ computed by the forward first difference method is due to the use of forward first differences, rather than centered first differences (see section b of this appendix). In contrast to the errors of the potential density method shown in Fig. B3a, the errors of the forward first difference method are more nearly uniform geographically. The bias is 4%–6% over most of the ocean, increasing to more than 8% in the western tropical Pacific Ocean where the vertical density gradients are stronger than anywhere else in the World Ocean at the depths where the NODC standard depths are coarsely spaced.

The geographical variability of differences between the Rossby radii shown in Fig. 6 and Rossby radii estimated by the hybrid method (forward first differences of potential density) applied to the 1994 NODC hydrographic data is shown in Fig. B6 and a histogram of these differences is shown in Fig. B4c. The systematic low bias of $\lambda_1$ computed by the hybrid method is attributable to a combination of the use of the gradient of potential density, rather than the neutral density gradient, and forward first differences, rather than centered first differences (see section c of this appendix). The combined effects of these two errors result in Rossby radii that are typically biased 10%–14% low, with errors exceeding 16% in the eastern North Atlantic and at high southern latitudes.

Picaut and Sombardier (1993) also noted a negative bias of $c_1$ computed numerically from standard-depth data compared with the values computed from high-resolution density profiles. They attributed the bias to an inability of standard-depth data to resolve the vertical structure of $N^2(z)$ and recommended increasing their published values of $\lambda_1$ by 8%. The simulation in section b of appendix C clarifies that the component of the bias in Fig. B6 associated with the use of standard-depth data is actually attributable to numerical errors arising from the use of forward first differences; the values of $\lambda_1$ and $c_1$ can be computed with sufficient accuracy from standard-depth hydrographic profiles if centered first differences are used. The analysis here reveals that even the estimates of $c_1$ computed by Picaut and Sombardier (1993) from high-resolution density profiles are biased low because of the use of the gradient of potential density rather than the neutral density gradient to estimate $N^2(z)$.

---

**APPENDIX C**

## 8. Numerical Solutions of the Eigenvalue Problem

### *a. Discretization of the eigenvalue problem*

The squared buoyancy frequency profile $N^2(z)$ was estimated at discrete depths $z = \zeta_k$ by the methods described in appendix B from the density profile $\rho(z)$ computed using the UNESCO (1981) equation of state from the NODC 1° × 1° climatological-average temperature and salinity values at the nonuniformly spaced standard depths $z_k$ listed in Table B1. In the centered first difference methods, the $\zeta_k$ are midway between standard depths $z_k$ and $z_{k+1}$. In the forward first difference methods, the $\zeta_k$ are equivalent to the standard depths $z_k$.

For the purposes of estimating the Rossby radii, negative estimates of $N^2(\zeta_k)$, presumably the result of noise in the climatological averaging and/or noise in the first derivatives of the density, were replaced with the estimate $N^2(\zeta_{k-1})$ at the next shallower depth $\zeta_{k-1}$; if $N^2(\zeta_1)$ at the shallowest level $\zeta_1$ was negative, it was replaced with a value of $10^{-8}$. The number of cases for which $N^2$ was negative was very small.

To assure that the full water column was represented, an additional discrete depth $z_k = -H$ was added to the density profile if the water depth $H$ was deeper than the deepest NODC standard depth at the center of that 1° × 1° location. In this case, the deepest value of $N^2(z)$ was set equal to the next shallower estimate between the deepest pair of NODC standard depths.

The eigenvalue problem (A.3) with boundary conditions (A.5) is the same form used by Emery et al. (1984), Houry et al. (1987), and Picaut and Sombardier (1993) to determine the first baroclinic gravity-wave phase speed $c_1$ and Rossby radius of deformation $\lambda_1$. To obtain solutions numerically, this eigenvalue problem must be discretized at the same nonuniformly spaced depths $\zeta_k$ at which $N^2(z)$ was estimated. A Taylor expansion of $\phi(z)$ about $z = \zeta_k$ yields

$$\phi(z) = \phi(\zeta_k) + (z - \zeta_k)\phi'(\zeta_k) + \frac{(z - \zeta_k)^2}{2!}\phi''(\zeta_k) + \cdots, \tag{C.1}$$

where the primes denote differentiation with respect to $z$. The value of $\phi''(\zeta_k)$ can be approximated by evaluating (C.1) at $\zeta_{k-1}$ and $\zeta_{k+1}$ and then scaling and differencing the resulting two equations to eliminate $\phi'(\zeta_k)$, yielding

$$\phi''(\zeta_k) = Q_k[D_{k+1}\phi(\zeta_{k-1}) - (D_k + D_{k+1})\phi(\zeta_k) + D_k\phi(\zeta_{k+1})], \tag{C.2}$$

where

$$D_k \equiv \zeta_k - \zeta_{k-1} \tag{C.3}$$

and

$$Q_k \equiv 2[D_kD_{k+1}(D_k + D_{k+1})]^{-1}. \tag{C.4}$$

Substituting (C.2) into the eigenvalue problem (A.3) then yields a set of discrete equations at the depths $\zeta_k$, expressed entirely in terms of $\phi$ at the same set of depths.

#### 1) CENTERED FIRST DIFFERENCES

In the centered first difference method, $N^2(z)$ is estimated at the $M - 1$ midpoints $z = z_{k+1/2}$, $k = 1, \ldots, M - 1$ between the $M$ nonuniformly spaced standard depths $z_k$ (see Fig. B1). The vertical velocity eigenfunctions $\phi(z)$ must therefore be discretized at the same midpoints, that is, $\zeta_k = z_{k+1/2}$ in the formalism above. Defining $\zeta_0 = z_1 = 0$ and $\zeta_M = z_M = -H$ in

(C.2) and (C.3) and applying the rigid-lid and flat-bottom boundary conditions (A.5) in the top and bottom discrete equations yields $M - 1$ equations that can be written in matrix eigenvalue form as

$$\mathbf{Q}^{\mathrm{T}}\,\mathbf{A}\Phi = \mu\Phi, \tag{C.5}$$

where, using (A.7),

$$\mu = -\frac{1}{c^2} = \begin{cases} -\dfrac{1}{f^2\lambda^2} & \text{if } \vartheta \gtrsim 5^\circ \\ -\dfrac{1}{4\beta^2\lambda^4} & \text{if } \vartheta \lesssim 5^\circ \end{cases} \tag{C.6}$$

is the eigenvalue corresponding to baroclinic gravity-wave phase speed $c$ and Rossby radius of deformation $\lambda$, $\Phi$ is the $(M - 1) \times 1$ column vector of the corresponding vertical velocity eigenfunction

$$\Phi = \begin{pmatrix} \phi(\zeta_1) \\ \vdots \\ \phi(\zeta_{M-1}) \end{pmatrix}, \tag{C.7}$$

$\mathbf{Q}$ is the $(M - 1) \times (M - 1)$ diagonal matrix

$$\mathbf{Q} = \begin{pmatrix} Q_1/N^2(\zeta_1) & 0 & & 0 \\ 0 & Q_2/N^2(\zeta_2) & & 0 \\ & & \ddots & \\ 0 & 0 & & Q_{M-1}/N^2(\zeta_{M-1}) \end{pmatrix}, \tag{C.8}$$

and $\mathbf{A}$ is the $(M - 1) \times (M - 1)$ tridiagonal matrix

$$\mathbf{A} = \begin{pmatrix} -(D_1 + D_2) & D_1 & 0 & & 0 \\ D_3 & -(D_2 + D_3) & D_2 & & 0 \\ 0 & D_4 & -(D_3 + D_4) & & 0 \\ & & & \ddots & \\ 0 & 0 & 0 & & -(D_{M-1} + D_M) \end{pmatrix}. \tag{C.9}$$

From (C.3) and the definitions $\zeta_0 = 0$ and $\zeta_M = z_M$, the $D_k$ in (C.9) and in the expression (C.4) for the $Q_k$ in (C.8) are

$$D_k = \begin{cases} z_2/2, & k = 1 \\ (z_{k+1} - z_{k-1})/2, & k = 2, \cdots, M - 1 \\ (z_M - z_{M-1})/2, & k = M. \end{cases} \tag{C.10}$$

The matrix equation(C.5) was solved for the $M - 1$ eigenvalues $\mu$ and corresponding eigenvectors $\Phi$ using a standard matrix eigenvalue routine. The first baroclinic gravity-wave phase speed $c_1$ and Rossby radius $\lambda_1$ were then obtained from the eigenvalue $\mu_1$ from (C.6). It should be noted that there are $M$ sample depths but only $M - 1$ eigenvalues and eigenfunctions. The barotropic eigensolution is eliminated in the quasigeostrophic potential vorticity equation for the vertical velocity.

2) FORWARD FIRST DIFFERENCES

In the forward first difference method, $N^2(z)$ is estimated at the $M - 1$ nonuniformly spaced standard depths $z_k$, $k = 1, \cdots, M - 1$ (see Fig. B1). The vertical velocity eigenfunctions $\Phi(z)$ must therefore be discretized at the same depths, that is, at $\zeta_k = z_k$ in the preceding formalism for the discretized eigenvalue problem. In this case, $\Phi''$ cannot be evaluated from

(C.2) at the top level $z_1$ since $z_0$ is undefined. The eigenvalue equation can therefore be discretized only at the $M - 2$ discrete depths $z_k$, $k = 2, \cdots, M - 1$. The matrix equations are therefore reduced to order $M - 2$ in the forward first difference method.

Defining $\zeta_M = z_M = -H$ as in the centered first difference method summarized above and applying the rigid-lid and flat-bottom boundary conditions (A.5) in the discrete equations for depths $z_2$ and $z_{M-1}$, the $M - 2$ equations can be written in the matrix eigenvalue form (C.5) as before, where $\Phi$ in this case is the $(M - 2) \times 1$ column vector of the vertical velocity eigenfunction

$$\Phi = \begin{pmatrix} \phi(z_2) \\ \vdots \\ \phi(z_{M-1}) \end{pmatrix}, \qquad \text{(C.11)}$$

**Q** is the $(M - 2) \times (M - 2)$ diagonal matrix

$$\mathbf{Q} = \begin{pmatrix} Q_2/N^2(z_2) & 0 & \cdots & 0 \\ 0 & Q_3/N^2(z_3) & & 0 \\ \vdots & & \ddots & \vdots \\ 0 & 0 & \cdots & Q_{M-1}/N^2(z_{M-1}) \end{pmatrix}, \qquad \text{(C.12)}$$

and **A** is the $(M - 2) \times (M - 2)$ tridiagonal matrix

$$\mathbf{A} = \begin{pmatrix} -(D_2 + D_3) & D_2 & 0 & \cdots & 0 \\ D_4 & -(D_3 + D_4) & D_3 & & 0 \\ 0 & D_5 & -(D_4 + D_5) & & 0 \\ \vdots & & & \ddots & \vdots \\ 0 & 0 & 0 & \cdots & -(D_{M-1} + D_M) \end{pmatrix}. \qquad \text{(C.13)}$$

The $D_k$ in (C.13) and in the expression (C.4) for the $Q_k$ in (C.12) are

$$D_k = z_k - z_{k-1}, \qquad k = 2, \cdots, M - 1. \qquad \text{(C.14)}$$

Implementation of the forward first difference discretized eigenvalue problem in the manner summarized above based on $N^2(z)$ estimated from the neutral density gradient as described in section b of appendix B yielded baroclinic Rossby radii that were very nearly identical to those published for the South Atlantic and portions of the North Atlantic and Indian Ocean by Houry et al. (1987). The small differences of order 1% are easily attributable to the differences between the Levitus (1982) hydrographic dataset used by Houry et al. (1987) and the 1994 NODC hydrographic dataset used here.

### *b. Case study comparisons of centered and forward first difference solutions*

The importance of the method of estimating the $N^2(z)$ profile can be quantified by a simple simulation. The first baroclinic Rossby radius of deformation $\lambda_1$ was computed numerically as described in section a of this appendix from $N^2(z)$ profiles estimated as described in appendix B using various discretization intervals. For all profiles considered, a resolution of 5 m was retained in the upper 200 m, where the vertical scales of $N^2(z)$ are short. The simulated resolution in deeper water ranged from 5 m to 200 m. The Rossby radii computed from a vertical resolution of 100 m are effectively equivalent to the Rossby radii computed from the NODC standard depth spacing, which is 100 m in the permanent pycnocline (see Table B1). For present purposes, the value of $\lambda_1$ computed for the neutral density gradient by (B.4) with the highest vertical resolution of 5 m throughout the water column was considered to be the"true" value. The biases of $\lambda_1$ computed with other simulated vertical resolutions and by the other methods summarized in appendix B were then defined to be the differences from this true value, expressed as a percentage of this true value.

The results of this simulation are shown in Fig. C1 for three geographical locations. It is evident from the figure that

the $\lambda_1$ based on $N^2(z)$ computed from the neutral density gradient by (B.4) are insensitive to the vertical resolution of the density profile; at all three locations, the computed values of $\lambda_1$ agree with the true values to within a fraction of a percent, regardless of the vertical resolution of the density profile. The first baroclinic Rossby radii estimated in section 3a by the neutral density gradient method from the NODC standard-depth hydrographic profiles are therefore not significantly different from those that would be estimated from essentially continuous hydrographic profiles.

The values of $\lambda_1$ computed from $N^2(z)$ estimated by the potential density method (B.1) are also insensitive to the vertical resolution. However, the resulting $\lambda_1$ for the cases considered in Fig. C1 are biased 8% low at the tropical and subpolar locations and 10% low at the midlatitude location. As discussed in section a of appendix B, these biases arise from the use of the gradient of potential density rather than the neutral density gradient to estimate $N^2(z)$. The geographical variability of this negative bias depends on the specific water masses sampled by the hydrographic profile (see section e of appendix B).

In contrast to the insensitivity of the centered first difference methods (B.1) and (B.4) to the vertical resolution of the density profile, the negative bias of $\lambda_1$ computed from $N^2(z)$ estimated by the forward first difference method (B.2) increases in magnitude with increased vertical spacing between the density samples. The dependence on vertical resolution indicates that these biases are purely a numerical problem arising from the use of forward first differences rather than centered first differences to estimate the density derivative in the expression (A.4) for $N^2(z)$. The forward first differences and centered first differences converge to the same value as the discrete sample spacing decreases. The forward first difference estimates of $\lambda_1$ with 5-m vertical resolution are essentially identical to the true values at all three locations. The magnitude of the negative bias of forward first difference estimates of $\lambda_1$ computed from standard-depth density profiles varies somewhat geographically, depending on the shape of the permanent thermocline (see section e of appendix B).

The negative biases of $\lambda_1$ (and hence $c_1$) computed by the hybrid method (B.3) also increase in magnitude with increased vertical spacing between the density samples. This is to be expected since this method estimates $N^2(z)$ from forward first differences. This component of the error in the hybrid method can be eliminated by using centered first differences. However, the resulting estimates of $\lambda_1$ agree with the values obtained by the potential density method, which are biased low relative to the true values as noted above because of the use of the gradient of potential density rather than the neutral density gradient to estimate $N^2(z)$.

We conclude that $\lambda_1$ and $c_1$ can be computed with sufficient accuracy from standard-depth hydrographic profiles if the neutral density gradient and centered first differences are used.

---

## Tables

Table 1. The parameters of the least squares estimate $\hat{\lambda}_1$ of the zonally averaged first baroclinic Rossby radius of deformation in kilometers obtained by regression onto a quadratic function of inverse latitude for the latitude range 10°–60°. The form of the quadratic function is $\hat{\lambda}_1(\vartheta) = a_0 + a_1\vartheta^{-1} + a_2\vartheta^{-2}$, where $\vartheta$ is the absolute value of latitude. The coefficients $a_0$, $a_1$, $a_2$ and the root-mean-square and maximum error of the regression fit are listed separately for each hemisphere for the global ocean (see Fig. 7), the Pacific Ocean, the Atlantic Ocean, and the Indian Ocean.

| | $a_0$ | $a_1$ | $a_2$ | rms (km) | max (km) |
|---|---|---|---|---|---|
| Global Ocean | | | | | |
| Northern Hemisphere | −17.13 | 1908.41 | −7572.13 | 1.69 | 4.34 |
| Southern Hemisphere | −12.79 | 1641.09 | −4827.22 | 1.45 | 2.74 |
| Pacific Ocean | | | | | |
| Northern Hemisphere | −14.77 | 1866.03 | −6809.97 | 1.17 | 2.67 |
| Southern Hemisphere | −6.89 | 1396.94 | −2587.56 | 1.12 | 2.46 |
| Atlantic Ocean | | | | | |
| Northern Hemisphere | −18.66 | 1902.66 | −8285.09 | 2.57 | 6.55 |
| Southern Hemisphere | −15.05 | 1673.95 | −6075.50 | 2.44 | 4.77 |
| Indian Ocean | | | | | |
| Northern Hemisphere | −13.90 | 1376.39 | −1833.22 | 1.00 | −2.62 |
| Southern Hemisphere | −20.05 | 1994.46 | −7500.20 | 3.57 | 4.57 |

Click on thumbnail for full-sized image.

Table B1. The standard depths in meters in the NODC climatological average hydrographic dataset.

| | | |
|---|---|---|
| 0 | 300 | 1400 |
| 10 | 400 | 1500 |
| 20 | 500 | 1750 |
| 30 | 600 | 2000 |
| 50 | 700 | 2500 |
| 75 | 800 | 3000 |
| 100 | 900 | 3500 |
| 125 | 1000 | 4000 |
| 150 | 1100 | 4500 |
| 200 | 1200 | 5000 |
| 250 | 1300 | 5500 |

Click on thumbnail for full-sized image.

---

## Figures

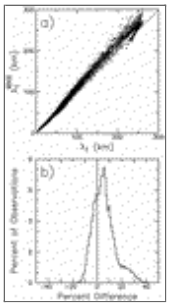

Click on thumbnail for full-sized image.

Fig. 1. Comparison between the WKB approximations $\lambda^{WKB}_1$ and numerical estimates $\lambda_1$ of the first baroclinic Rossby radius of deformation on a global 1° × 1° grid. (a) Scatterplot of $\lambda^{WKB}_1$ versus $\lambda_1$. The dashed line represents the line of perfect agreement. The slope of the least squares fit line through the origin is 1.065, indicating the WKB estimates are biased high by 6.5%, on average. (b) Histogram of the differences ($\lambda^{WKB}_1 - \lambda_1$), expressed as a percentage of $\lambda_1$.

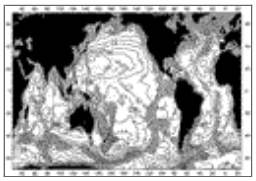

Click on thumbnail for full-sized image.

Fig. 2. Global contour map of the 1° × 1° gridded first baroclinic gravity-wave phase speed $c_1$ (in m s$^{-1}$) computed numerically from the neutral density gradient by centered first differences. Water depths shallower than 3500 m are shaded.

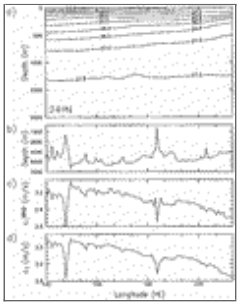

Click on thumbnail for full-sized image.

Fig. 3. Zonal sections along 24°N across the subtropical North Pacific of (a) the density expressed as $\sigma_\theta$ in the upper 2000 m of the water column, (b) the water depth $H$ in meters, (c) the WKB approximation $c^{WKB}_1$ for the first baroclinic gravity-wave phase speed in m s$^{-1}$, and (d) the numerical estimate of the first baroclinic gravity-wave phase speed $c_1$.

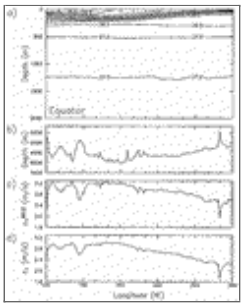

Click on thumbnail for full-sized image.

Fig. 4. As in Fig. 3 except along the equator in the Pacific.

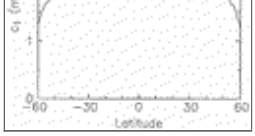

Click on thumbnail for full-sized image.

Fig. 5. The global zonally averaged first baroclinic gravity-wave phase speed $c_1$ (in m s$^{-1}$) obtained from the 1° gridded $c_1$ shown in Fig. 2.

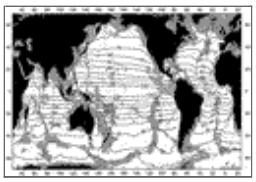

Click on thumbnail for full-sized image.

Fig. 6. Global contour map of the 1° × 1° first baroclinic Rossby radius of deformation $\lambda_1$ in kilometers computed by Eq. (2.3) from the first baroclinic gravity-wave phase speed shown in Fig. 2. Water depths shallower than 3500 m are shaded.

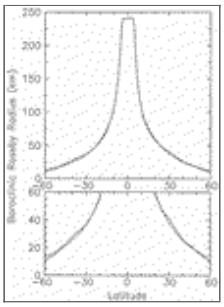

Click on thumbnail for full-sized image.

Fig. 7. The global zonally averaged first-baroclinic Rossby radius of deformation $\lambda_1$ in kilometers (solid line) obtained from the 1° × 1° gridded Rossby radii shown in Fig. 6. The *y* axis is expanded in the lower panel to resolve the middle- and high-latitude Rossby radii better. The dashed lines represent least squares fits over the latitude range 10°–60° to an empirical quadratic function of inverse latitude; the parameters of the least squares estimates are listed in Table 1. Least squares fit parameters for each individual ocean basin are listed in Table 1.

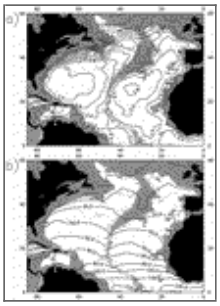

Click on thumbnail for full-sized image.

Fig. 8. North Atlantic maps of (a) the first baroclinic gravity-wave phase speed $c_1$ (in m s$^{-1}$) and (b) the first baroclinic Rossby radius of deformation $\lambda_1$ in kilometers computed from the Lozier et al. (1995) (LOC) 1° × 1° gridded climatological-average hydrographic data. Gray shading represents water shallower than 3500 m.

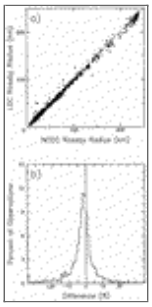

Click on thumbnail for full-sized image.

Fig. 9. Comparison between numerical estimates of the first baroclinic Rossby radius of deformation computed from the NODC and the LOC climatological-average hydrographic datasets. (a) Scatterplot of LOC versus NODC. The dashed line represents the line of perfect agreement. (b) Histogram of the differences LOC minus NODC, expressed as a percentage of the LOC estimate.

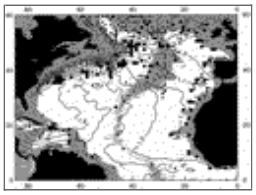

Click on thumbnail for full-sized image.

Fig. 10. The 1° × 1° locations at which the Rossby radius differences LOC minus NODC are greater than 10% of the LOC estimate (large dots) and less than −10% of the LOC estimate (small dots). Contours represent the dynamic height of the sea surface relative to 1000 m in units of meters.

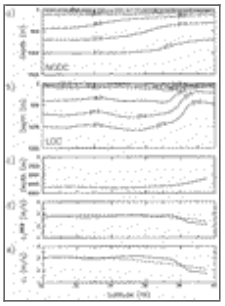

Click on thumbnail for full-sized image.

Fig. 11. Meridional sections along 67.5°W across the Gulf Stream of (a) the density expressed as $\sigma_\theta$ computed from the NODC climatological average hydrographic data in the upper 1500 m of the water column, (b) the density expressed as $\sigma_\theta$ computed from the LOC climatological average hydrographic data, (c) the water depth $H$ in meters, (d) the WKB approximations $c^{\mathrm{WKB}}_1$ for the first baroclinic gravity-wave phase speeds (in m $s^{-1}$) computed from the NODC (dashed line) and LOC (solid line) datasets, and (e) numerical estimates of the baroclinic gravity-wave phase speed $c_1$ computed from the NODC (dashed line) and LOC (solid line) datasets.

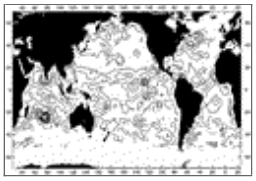

Click on thumbnail for full-sized image.

Fig. 12. Contour plot of the amplitudes of least squares fits of the 1° × 1° Rossby radii for the 12 monthly climatological-average NODC density profiles to an annual harmonic. The amplitudes are expressed as a percentage of the annual mean first baroclinic Rossby radius shown in Fig. 6. The contour interval is 1%.

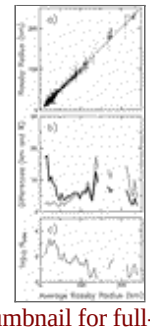

Click on thumbnail for full-sized image.

Fig. 13. (a) Scatterplot of the first baroclinic Rossby radius of deformation computed from each individual hydrographic profile in the North Atlantic quality-controlled LOC 86-yr hydrographic dataset, shown as a function of the climatological average Rossby radius computed from the nearest 1° × 1° LOC grid location. (b) Root-mean-square differences of the individual Rossby radii from the climatological average Rossby radii expressed in kilometers (thin solid line) and expressed as a percentage of the climatological average Rossby radii (thick solid line). Statistics were computed from panel (a) over bin sizes of 5 km. (c) Logarithm of the number of individual hydrographic profiles in each 5-km bin over which the statistics in panel (b) were computed.

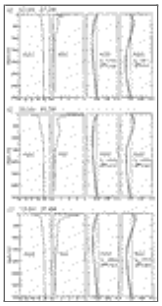

Click on thumbnail for full-sized image.

Fig. A1. Vertical profiles of density expressed as $\sigma_\theta$, buoyancy frequency $N(z)$ in cycles per hour, and the WKB approximations (thin solid lines) and numerical estimates (heavy solid lines) for the first and second baroclinic vertical velocity eigenfunctions $\Phi_1$ and $\Phi_2$ at three locations in the middle of the North Atlantic: (a) 53.0°N, 27.2°W; (b) 29.9°N, 45.3°W; and (c) 13.9°N, 37.6°W. The WKB approximations $\lambda^{WKB}_m$ and numerical estimates $\lambda_m$ for the Rossby radii in kilometers are labeled on each eigenfunction plot.

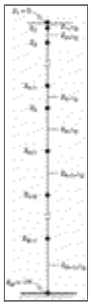

Click on thumbnail for full-sized image.

Fig. B1. A schematic vertical profile of the $M$ standard depths $z_k$ in the NODC climatological average hydrographic dataset from which the buoyancy frequency profile $N(z)$ is estimated in order to solve the eigenvalue equation for the Rossby radius of deformation. The depth $z_k + 1/2$ corresponds to the midpoint between standard depths $z_k$ and $z_k + 1$. The actual NODC standard depths are listed in Table B1.

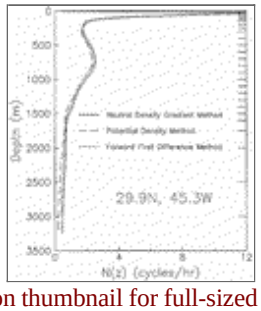


Click on thumbnail for full-sized image.

Fig. B2. Profiles of $N(z)$ in cycles per hour estimated from the standard-depth climatological average density profile shown in Fig. A1b by the potential density method (dashed line), the forward first difference method (dotted line), and the neutral density gradient method. The tick marks along the right axis indicate the NODC standard depths.

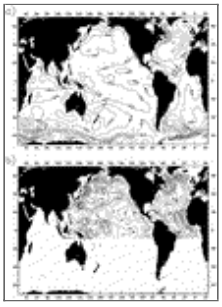

Click on thumbnail for full-sized image.

Fig. B3. Smoothed global contour maps of (a) the errors of the 1° × 1° gridded first baroclinic Rossby radius computed numerically from the 1994 NODC hydrographic dataset by the potential density method, and (b) the differences between the actual Emery et al. (1984) 5° × 5° gridded first baroclinic Rossby radius and the 1° × 1° gridded values of the Rossby radius shown in Fig. 6 at the center locations of the Emery et al. 5° × 5° squares. The errors are expressed as a percentage of the first

baroclinic Rossby radius shown in Fig. 6, and the sign convention is such that negative values (represented by dashed contours) correspond to estimates biased low compared with the values shown in Fig. 6.

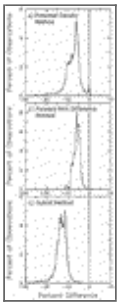

Click on thumbnail for full-sized image.

Fig. B4. Histograms of the percentage errors of (a) the potential density method shown in Fig. B3a, (b) the forward first difference method shown in Fig. B5, and (c) the hybrid method shown in Fig. B6.

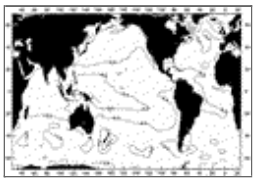

Click on thumbnail for full-sized image.

Fig. B5. Smoothed global contour map of the errors of the 1° × 1° gridded first baroclinic Rossby radius computed numerically from the 1994 NODC hydrographic dataset by the forward first difference method. The errors are expressed as a percentage of the first baroclinic Rossby radius shown in Fig. 6. The sign convention is the same as in Fig. B3.

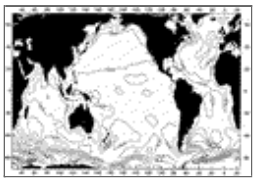

Click on thumbnail for full-sized image.

Fig. B6. Smoothed global contour map of the errors of the 1° × 1° gridded first baroclinic Rossby radius computed numerically from the 1994 NODC hydrographic dataset by the hybrid method. The errors are expressed as a percentage of the first baroclinic Rossby radius shown in Fig. 6. The sign convention is the same as in Fig. B3.

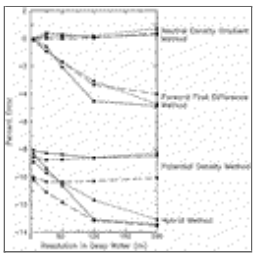

Click on thumbnail for full-sized image.

Fig. C1. The percentage errors of numerical estimates of $\lambda_1$ as a function of the vertical resolution of discretely sampled density profiles (see text in section b of appendix C for details) based on $N^2(z)$ estimated by the various methods considered in this study. Solid, dashed, and dotted lines correspond to the locations of the density profiles shown in Figs. A1a, A1b, and A1c, respectively.

*Corresponding author address:* Dr. Dudley B. Chelton, College of Oceanic and Atmospheric Sciences, Oregon State University, 104 Ocean Admin. Building, Corvallis, OR 97331-5503.

E-mail: chelton@oce.orst.edu

[1] Digital files of the 1° × 1° gridded fields of $c_1$ and $\lambda_1$ shown in Figs. 2 and 6 can be obtained via the Internet by contacting the corresponding author by e-mail at chelton@oce.orst.edu.

top


Headquarters: 45 Beacon Street Boston, MA 02108-3693
DC Office: 1120 G Street, NW, Suite 800 Washington DC, 20005-3826
amsinfo@ametsoc.org Phone: 617-227-2425 Fax: 617-742-8718
Allen Press, Inc. assists in the online publication of *AMS* journals.